Observation and analysis of shear instability in the Fraser River estuary

E. W. Tedford,[1] J. R. Carpenter,[1] R. Pawlowicz,[2] R. Pieters,[2] and G. A. Lawrence[1]

Received 2 February 2009; revised 1 May 2009; accepted 14 July 2009; published 4 November 2009.

[1] We investigate the occurrence of shear instability in the Fraser River estuary. Instabilities observed with an echo sounder are compared with a linear stability analysis based on observed velocity and density profiles. We find that each set of observed instabilities coincides with an unstable mode predicted by the Taylor-Goldstein equation. Each of these instabilities occurs in a region where the gradient Richardson number is less than the critical value of 1/4. Both the Taylor-Goldstein predictions and the echo soundings indicate the instabilities are concentrated either above or below the density interface. This ''one sidedness'' is in contrast to the archetypal Kelvin-Helmholtz instability. Although the dominant source of mixing in the estuary appears to be caused by shear instability, when the tide produces strong near-bed velocities, small-scale overturning due to boundary layer turbulence is apparent throughout the depth.

Citation: Tedford, E. W., J. R. Carpenter, R. Pawlowicz, R. Pieters, and G. A. Lawrence (2009), Observation and analysis of shear instability in the Fraser River estuary, *J. Geophys. Res.*, *114*, C11006, doi:10.1029/2009JC005313.

1. Introduction

[2] Shear instabilities occur in highly stratified estuaries and can influence the large-scale dynamics by redistributing mass and momentum. Specifically, shear instabilities have been found to influence salinity intrusion in the Fraser River estuary [*Geyer and Smith*, 1987; *Geyer and Farmer*, 1989; *MacDonald and Horner-Devine*, 2008]. We describe recent observations in this estuary and examine the shear and stratification that lead to instability. The influence of long time scale processes such as freshwater discharge and the tidal cycle are also discussed.

[3] Rather than relying on a bulk or gradient Richardson number to assess stability we use numerical solutions of the Taylor-Goldstein (TG) equation based on observed profiles of velocity and density. This approach has been used with some success in the ocean [e.g., *Moum et al.*, 2003] but, with the exception of the simplified application by *Yoshida et al.* [1998], has not been applied in estuaries. Solving the TG equation provides the growth rate, wavelength, phase speed and mode shape of the instabilities. We compare these predicted wave properties with instabilities observed using an echo sounder.

[4] *Geyer and Farmer* [1989] found that instabilities in the Fraser River estuary were most apparent during ebb tide when strong shear occurred over the length of the salinity intrusion. They outlined a progression of three phases of increasingly unstable flow that occurs over the course of the ebb. In the first phase, strain sharpens the density interface; shear is stronger than during flood, but insufficient to cause shear instability. In the second phase, the lower layer reverses and shear between the fresh and saline layers increases. Shear instability and turbulent mixing are concentrated at the pycnocline rather than in the bottom boundary layer. By the third phase of the ebb, shear instability has completely mixed the two layers leaving homogeneous water throughout the depth. During flood there is some mixing, however it is concentrated at the front located at the landward tip of the salinity intrusion. Similarly, *MacDonald and Horner-Devine* [2008], studying mixing at high freshwater discharge (7000 m^3s^{-1}), found that two to three times more mixing occurred during ebb tide than during flood. The present analysis is focused on the ebb tide at high and low freshwater discharge, although some results during flood tide are also presented.

[5] The paper is organized as follows. The setting and field methods are described in section 2. The general structure of the salinity intrusion is described in section 3. In section 4 we present the background theory needed to perform stability analysis in the Fraser River estuary. In section 5 predictions from the stability analysis are compared with observations. In section 6 the source of relatively small-scale overturning is briefly discussed. In section 7 the results of the stability analysis are discussed followed by conclusions in section 8.

2. Field Program

2.1. Site Description and Data Collection

[6] Data were collected in the main arm of the Fraser River estuary, British Columbia, Canada (Figure 1). The estuary is 10 to 20 m deep with a channel width of 600 to 900 m. Cruises were conducted on 12, 14, and 21 June 2006 and 10 March 2008. Here we present one transect from each of the June 2006 cruises and three transects from the March

[1]Department of Civil Engineering, University of British Columbia, Vancouver, British Columbia, Canada.
[2]Department of Earth and Ocean Sciences, University of British Columbia, Vancouver, British Columbia, Canada.

0148-0227/09/2009JC005313$09.00

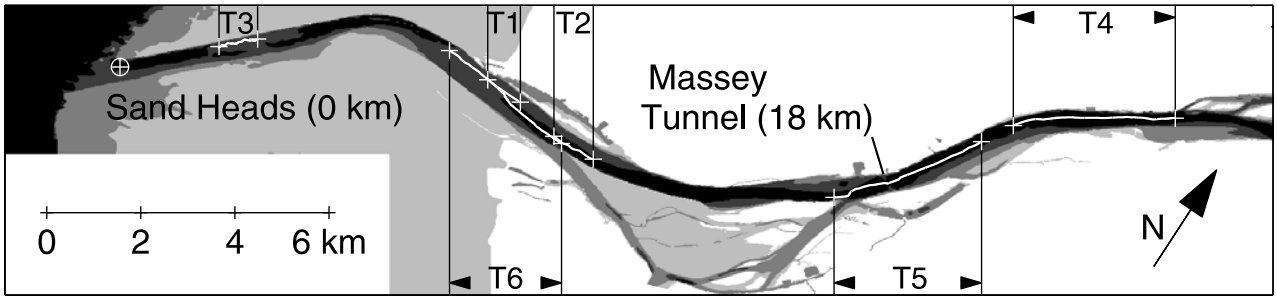

Figure 1. Map of the lower 27 km of the Fraser River. The locations of the six transects are marked T1–T6. The mouth of the river (Sand Heads) is located at 49° 6′ N and 123° 18′ W.

2008 cruise (see Table 1). The freshwater discharge during the June 2006 transects was typical of the freshet at approximately 6000 m^3s^{-1}. During the March 2008 transects, freshwater discharge was near the annual minimum at 850 m^3s^{-1}. In June 2006, transects were made during both ebb and flood tide. In March 2008, transects cover most of a single ebb tide (Figure 2). The tides in the Strait of Georgia have $M2$ and $K1$ components of similar amplitude (approximately 1 m) resulting in strong diurnal variations. The tidal range varies from approximately 2 m during neap tides to approximately 4.5 m during spring tides. During both the 2006 and 2008 observations the tidal range was approximately 3 m.

[7] The distance salinity intrudes landward of Sand Heads, i.e., the total length of the salinity intrusion, varies considerably with tidal conditions and freshwater discharge. *Ward* [1976] found the maximum length of the intrusion occurred just after high tide and varied from 8 km at high discharge (9000 m^3s^{-1}) to 31 km at low discharge (850 m^3s^{-1}). *Geyer and Farmer* [1989] found that, at average discharge (3000 m^3s^{-1}), the maximum length of the intrusion matched the horizontal excursion of the tides (10 to 20 km) and, similar to *Ward* [1976], occurred just after high tide. *Kostachuk and Atwood* [1990] found that the minimum length of the salinity intrusion typically occurred 1 h after low tide. The longest intrusion they observed at low tide was approximately 20 km. They predicted that complete flushing of salt from the estuary would occur on most days during the freshet (freshwater discharge >5000 m^3s^{-1}).

2.2. Field Methods

[8] Data along the six transects were collected by drifting seaward with the surface flow while logging velocity and echo sounder data and yoyoing a conductivity-temperature-depth (CTD) profiler. The velocity measurements were made with a 1200 kHz RDI acoustic Doppler current profiler (ADCP) sampling at 0.4 Hz with a vertical resolution of 250 mm. The velocities were averaged over 60 s to remove high-frequency variability. The echo soundings were made with a 200 kHz Biosonics sounder sampling at 5 Hz with a vertical resolution of 18 mm. Profile data were collected with a Seabird 19 sampling at 2 Hz. Selected echo sounder, ADCP and CTD data are shown in Figure 3. As indicated by the superimposed density profiles, strong gradients in density are generally associated with a strong echo from the sounder.

[9] The CTD was profiled on a load bearing data cable that provided constant monitoring of conductivity, temperature and depth. These data allowed us to quickly identify the front of the salinity intrusion and avoid direct contact of the instrument with the bottom. To increase the vertical resolution of the profiles, the CTD was mounted horizontally with a fin to direct the sensors into the flow. In this configuration, the instrument was allowed to descend rapidly and then was raised slowly (0.2–0.4 m s^{-1}) relying on horizontal velocity of the water relative to the CTD to flush the sensors. The upcast, which had higher vertical resolution, was in reasonable agreement with the echo intensity from the sounder. On the few occasions that the higher-resolution upcast did not coincide with the appearance of instabilities in the echo sounder, we used the downcast. The total number of CTD casts we were able to perform varied from transect to transect depending on field conditions (surface velocity, shear, ship traffic, woody debris).

3. General Description of the Salinity Intrusion

[10] We observed important differences in the structure of the salinity intrusion between high and low freshwater discharge. At high discharge, our observations were similar to those described by *Geyer and Farmer* [1989], where the salinity intrusion had a two-layer structure resembling a classic salt wedge. At low discharge, however, the salinity intrusion exhibited greater complexity.

3.1. High Discharge

[11] During flood tide, mixing was concentrated near the steep front at the landward tip of the salt wedge (2.7–3.03 km in Figure 3c). During ebb tide, the steep front was replaced by a gently sloping pycnocline (Figure 3b, landward of 11.6 km) and there was no apparent concentration of mixing at the landward tip of the salt wedge (not shown).

[12] We will focus on the wave-like disturbances that occur on the pycnocline especially during ebb tide. The

Table 1. Details of Transects Shown in Figures 1 and 2[a]

Transect	Discharge (m^3 s^{-1})	Tide	x (km)	ΔU (m s^{-1})	$\Delta\rho$ (kg m^{-3})	h (m)	J
1	6400	ebb	8.6	1.6	14.3	5.2	0.29
2	6500	ebb	11	1.65	20	3.5	0.25
3	5700	flood	2.2	1.5	23.1	3.5	0.35
4	850	ebb	24.5	1.5	12.9	12	1.3
5	850	ebb	19	1.5	12.9	12	1.3
6	850	ebb	10.5	2.5	7.3	12	0.3

[a]The location indicates the distance upstream from the mouth (Sand Heads).

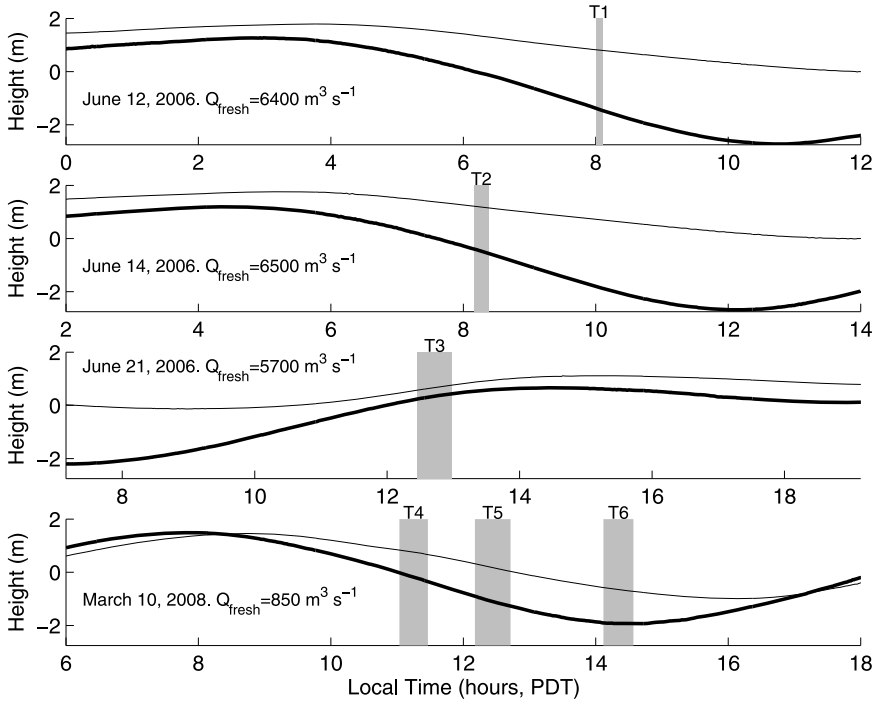

Figure 2. Observed tides at Point Atkinson (heavy line) and New Westminster (thin line) for the 4 days of field observations. The Point Atkinson data are representative of the tides in the Strait of Georgia beyond the influence of the Fraser River. New Westminster is located 37 km upstream of the mouth of the river at Sand Heads (see Figure 1). The records are both referenced to mean sea level at Point Atkinson. The duration of the six transects are marked T1–T6.

largest of these were observed during transect 1 (Figure 3a, 8.7 to 8.9 km, between depths of 3 and 10 m). These disturbances occurred within the upper layer as it passed over the nearly stationary water below a depth of 10 m. Smaller amplitude disturbances were observed during transect 2 (Figure 3b, 11.05 km). In our application of the TG equation we will show that disturbances like these are a result of shear instability.

[13] Not all of the disturbances on the pycnocline are a result of shear instability. For example, for most of the velocity and density profiles collected during transect 3 (Figure 3c) the TG equation does not predict instability. The disturbances seen from 2.5 to 3.0 km are caused by the large sand waves on the bottom (the thick black line in the echo sounding). The crests of the sand waves were typically 30 m apart and 1 to 2 m high, and were found over most of the river surveyed during high discharge (2.5 km to 15 km). During flood tide, flow over these sand waves caused particularly regular disturbances on the pycnocline.

3.2. Low Discharge

[14] At low discharge, at the beginning of the ebb, the front of the salinity intrusion was located between 28 and 30 km from Sand Heads. Unlike the observations at high discharge a well defined front was not visible in the echo sounder, and CTD profiles were needed to identify its location. Seaward of the front (Figure 4a), the echo sounder and the CTD profiles show a multilayered structure with more complexity than was observed at high discharge. At this early stage of the ebb, the CTD profiles generally show partially mixed layers separated by several weak density interfaces.

[15] Later in the ebb, during transect 5 (Figure 4b), near bottom velocities turn seaward and the velocity shear between the top and the bottom increases. At maximum ebb (transect 6, Figure 4c), the shear increases further, reaching a maximum of approximately 2.5 m s^{-1} over a depth of 12 m. Mixed water occurs at both the surface and the bottom resulting in an overall decrease in the vertical density gradient. By the time transect 6 is complete the ebb flow is decelerating. The salinity intrusion continues to propagate seaward until low tide but, given its length and velocity it does not have sufficient time to be completely flushed from the estuary. During the next flood the mixed water remaining in the estuary allows a complex density structure to develop similar to that seen early in the observed ebb. This differs from the behavior at high freshwater discharge when nearly all of the seawater is flushed completely from the estuary at least once a day.

4. Stability of Stratified Shear Flows

4.1. Taylor-Goldstein Equation

[16] Following *Taylor* [1931] and *Goldstein* [1931], we assess the stability of the flow by considering the evolution of perturbations on the background profiles of density and horizontal velocity, denoted here by $\rho(z)$ and $U(z)$, respectively. If the perturbations to the background state are sufficiently small they are well approximated by the linear equations of motion. It then suffices to consider sinusoidal perturbations, represented by the normal mode form $e^{ik(x-ct)}$, where x is the horizontal position and t is time. Here $k = 2\pi/\lambda$ is the horizontal wave number with λ the wavelength, $c = c_r + ic_i$ is the complex phase speed. If we further assume that

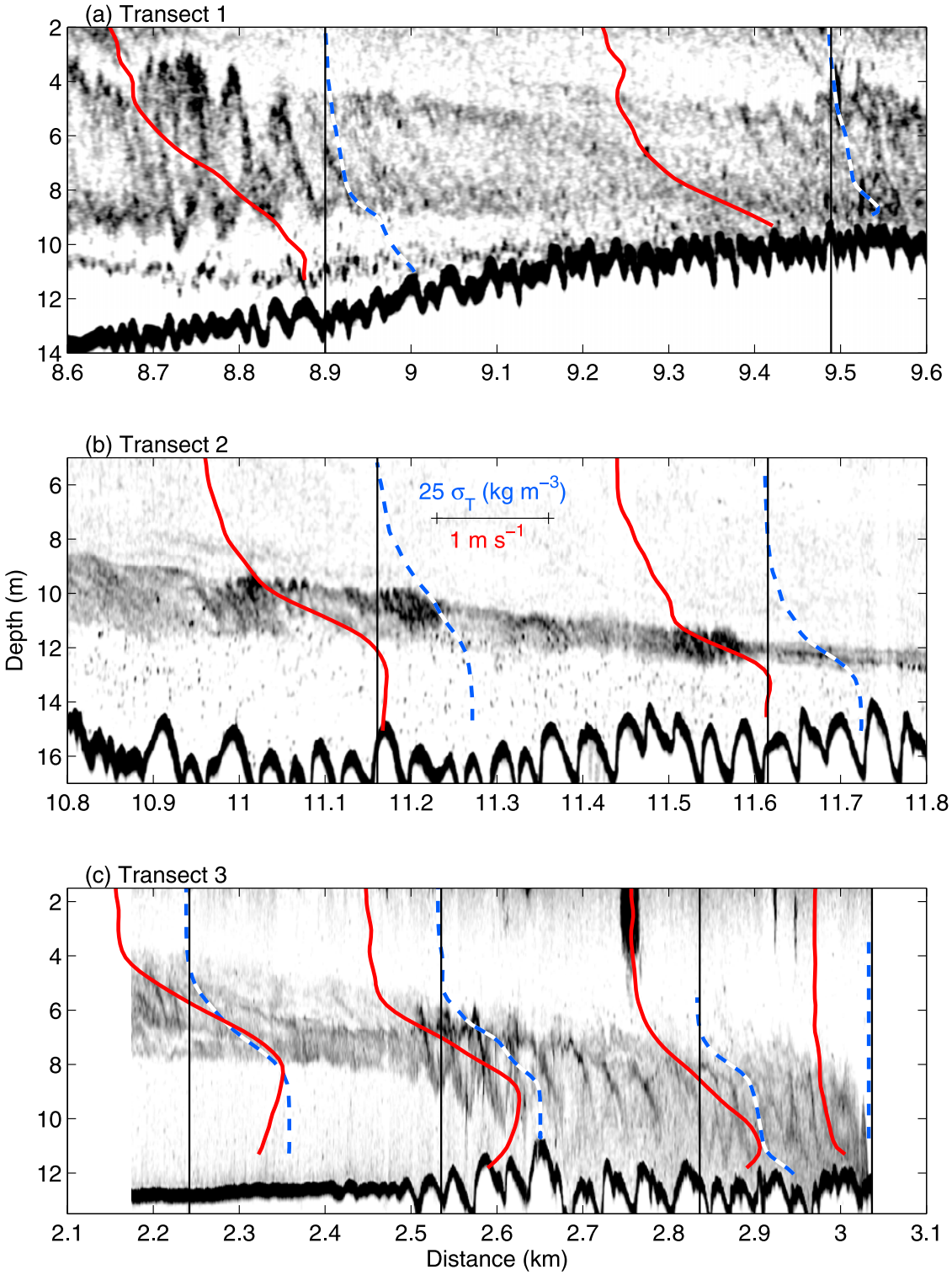

Figure 3. Echo soundings observed during high discharge on (a) transect 1, ebb tide; (b) transect 2, ebb tide; and (c) transect 3, flood tide. The shading scales with the log of the echo intensity with black corresponding to the strongest echoes. Selected velocity profiles (red) from the ADCP and density profiles (blue dashed) from the CTD are superimposed (not all are shown). The black line indicates the location of the boat in the middle of the cast, as well as the zero reference for the velocity and σ_t. The velocity profile was calculated as a 1 min average centered on the time of the CTD cast. The undulations in the bed of the river (thick black line at the bottom of the echo soundings) are a result of sand waves.

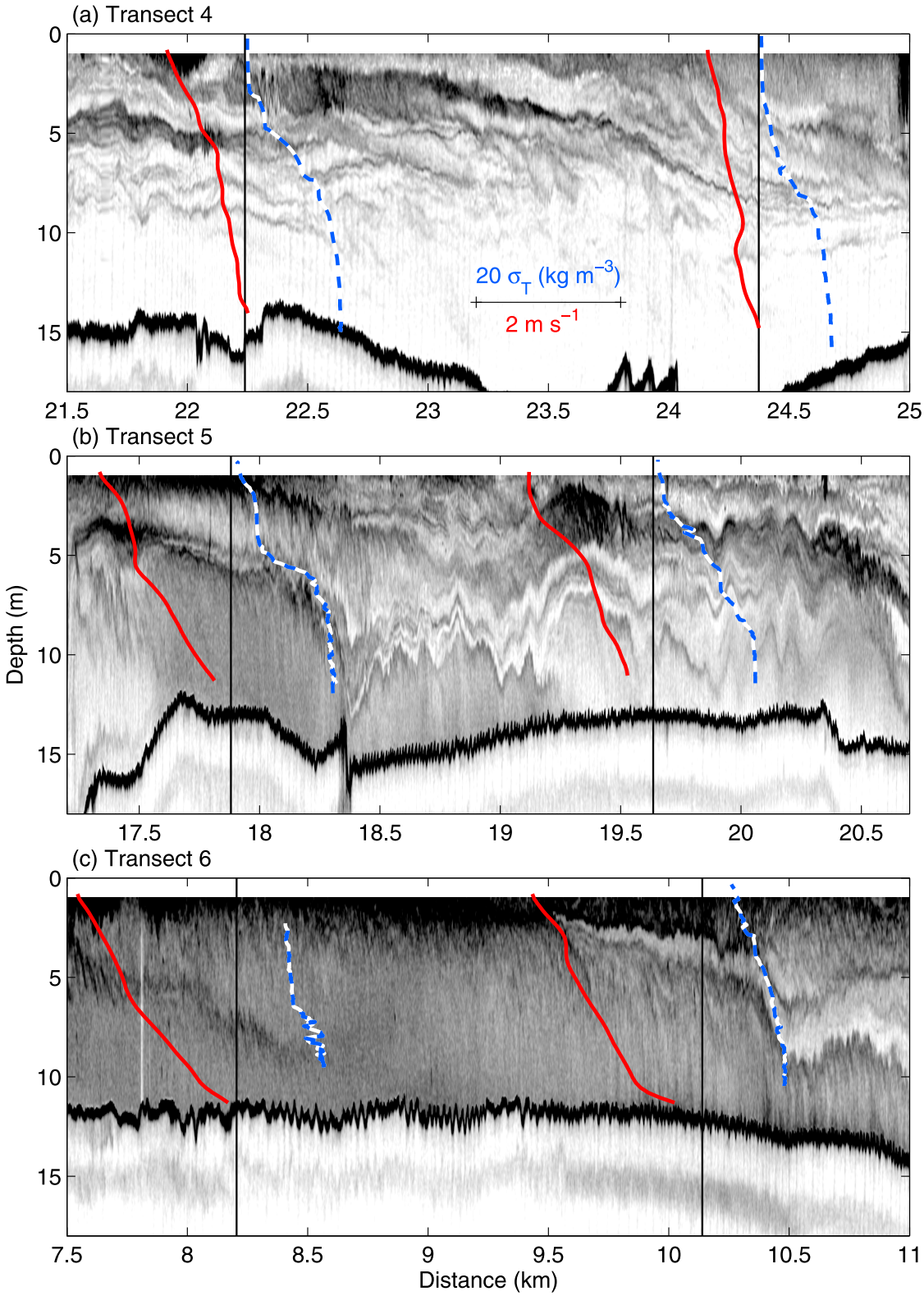

Figure 4. Echo soundings during low discharge observed during (a) transect 4, early ebb; (b) transect 5, mid ebb; and (c) transect 6, late ebb. The shading scales with the log of the echo intensity with black corresponding to the strongest echoes. Note that the scale of the shading is the same in Figures 4a–4c. Velocities (red) from the ADCP and densities (blue dashed) from the CTD are superimposed. The black line indicates the location of the boat in the middle of the cast, as well as the zero reference for the velocity and σ_t. The velocity profile was calculated as a 1 min average centered on the time of the CTD cast.

the flow is incompressible, Boussinesq, inviscid, and non-diffusive, we arrive at the Taylor-Goldstein (TG) equation

$$\frac{d^2\hat{\psi}}{dz^2} + \left[\frac{N^2}{(U-c)^2} - \frac{d^2U/dz^2}{U-c} - k^2\right]\hat{\psi} = 0, \quad (1)$$

where the stream function is given by $\psi(x, z, t) = \hat{\psi}(z)e^{ik(x-ct)}$ and $N^2(z) = -(g/\rho_0)(d\rho/dz)$ represents the Boussinesq form of the squared buoyancy frequency with a reference density, ρ_0.

[17] Solutions to the TG equation consist of eigenfunction-eigenvalue sets $\{\hat{\psi}(z), c\}$, for each value of k. Each set $\{\hat{\psi}(z), c\}$ is referred to as a mode, and the solution may consist of the sum of many such modes for a single k. The background flow, represented by $U(z)$ and $\rho(z)$, is then said to be unstable if any modes exist that have $c_i \neq 0$. In this case the small perturbations grow exponentially at a rate given by kc_i. In general, unstable modes are found over a range of k, and it is the mode with the largest growth rate that is likely to be observed. Although they are based on linear analysis, TG predictions of the wave properties, k and c, typically match those of finite amplitude instabilities observed in the laboratory [*Thorpe*, 1973; *Lawrence et al.*, 1991; *Tedford et al.*, 2009].

4.2. Miles-Howard Criterion

[18] A useful criterion to assess the stability of a given flow without solving the TG equation was derived by *Miles* [1961] and *Howard* [1961]. They found that if the gradient Richardson number, $Ri(z) = N^2/(dU/dz)^2$, exceeds 1/4 everywhere in the profile, then the TG equation has no unstable modes; that is, c_i must be zero for all modes. In other words, $Ri \geq 1/4$ everywhere is a sufficient condition for stability, referred to as the Miles-Howard criterion. Note that if $Ri < 1/4$ at some location, instability is possible, but not guaranteed.

[19] Despite the inconclusive nature of the Miles-Howard criterion for determining instability, it is often employed as a sufficient condition for instability in density stratified flows, and has been found to have reasonable agreement with observations [*Thorpe*, 2005, pp. 201–204]. Looking specifically at the Fraser River estuary, *Geyer and Smith* [1987] were able to compute statistics of Ri and show that decreases in Ri were accompanied by mixing in the estuary.

4.3. Mixing Layer Solution

[20] Since the TG equation is an eigenvalue problem with variable coefficients, analytical solutions can only be obtained for the simplest profiles, and recourse is usually made to numerical methods [e.g., *Hazel*, 1972]. However, the available analytical solutions are often a useful point of departure. We look at one such solution that closely approximates conditions found in the estuary during high discharge. This solution is based on the simple mixing layer model of Holmboe (described by *Miles* [1963]).

[21] In a general form of the model, the velocity and density profiles are represented by the hyperbolic tangent functions

$$U(z) = \frac{\Delta U}{2}\tanh\left(\frac{2(z-d)}{h}\right) \quad \text{and}$$
$$\rho(z) = -\frac{\Delta\rho}{2}\tanh\left(\frac{2z}{\delta}\right) + \rho_0. \quad (2)$$

where h is the shear layer thickness, δ is the thickness of the density interface. The parameter d allows for a vertical offset in the positions of the shear layer and density interface. In the simplest case the shear layer and density stratification have equal thickness, giving $R = h/\delta = 1$, and they coincide in their vertical positions so that the asymmetry $a = 2d/h = 0$. In this case, $Ri(z)$ is at its minimum at the center of the mixing layer ($z = 0$), and is equal to the bulk Richardson number $J = g\Delta\rho\, h/\rho_0\, (\Delta U)^2$. When the bulk Richardson number (i.e., the minimum Ri) drops below 1/4, flows with $R = 1$ and $a = 0$ become unstable. The resulting instabilities are of the Kelvin-Helmholtz (KH) type, in which the shear layer rolls up to form an array of billows that are stationary with respect to the mean flow, and which display large overturns in density [*Thorpe*, 1973].

[22] It is not generally the case that $J \geq 1/4$ results in stability. For example, if the density interface is relatively sharp ($R > 2$) an additional mode of instability, the Holmboe mode, is excited [*Alexakis*, 2005]. In this case, the range of J over which instability occurs extends above 1/4. That is, $Ri < 1/4$ somewhere in z at the same time as $J > 1/4$. While it is generally true that flows with higher J are subject to less mixing by shear instabilities, by itself, J does not indicate whether or not a flow is unstable.

[23] For simplicity, the analytical solution of Holmboe's mixing layer model assumes the flow is unbounded in the vertical. In our analysis we include boundaries at the top and bottom where $\hat{\psi}$ must satisfy the boundary condition $\hat{\psi} = 0$. The presence of these boundaries tends to extend the range of unstable wave number to longer wavelengths [*Hazel*, 1972]. However, in the cases considered here, at the wave number of maximum growth, the boundaries have little or no impact on k and c.

4.4. Solution of the TG Equation for Observed Profiles

[24] We use the numerical method described by *Moum et al.* [2003] to generate solutions to the TG equation based on measured velocity and density profiles. Whenever possible we use velocity and density profiles collected at the upstream edge of apparent instabilities in the echo soundings. The velocity profile, a 60 s average, is an average over one or more instabilities (the instabilities have periods <60 s). This averaging reduces the influence of individual instabilities on the velocity profile, which in the TG equation, is taken to represent the background velocity profile. The velocity profile is then smoothed in the vertical using a low-pass filter (removing vertical wavelengths <2 m). The density profile is smoothed by fitting a linear function, and one or more tanh functions (one for each density interface). By using smooth profiles we are effectively ignoring instability associated with small-scale variations in the profiles.

[25] Because the point of observation moves in time, i.e., the boat is drifting seaward, predicted wavelengths from the TG equation cannot be compared directly to the wavelength of instabilities as they appear in the echo soundings. The wavelength predicted with the TG solution must be shifted to account for the speed of the instabilities with respect to the speed of the boat:

$$\lambda^* = \left|\frac{v_b}{c_r - v_b}\right|\lambda. \quad (3)$$

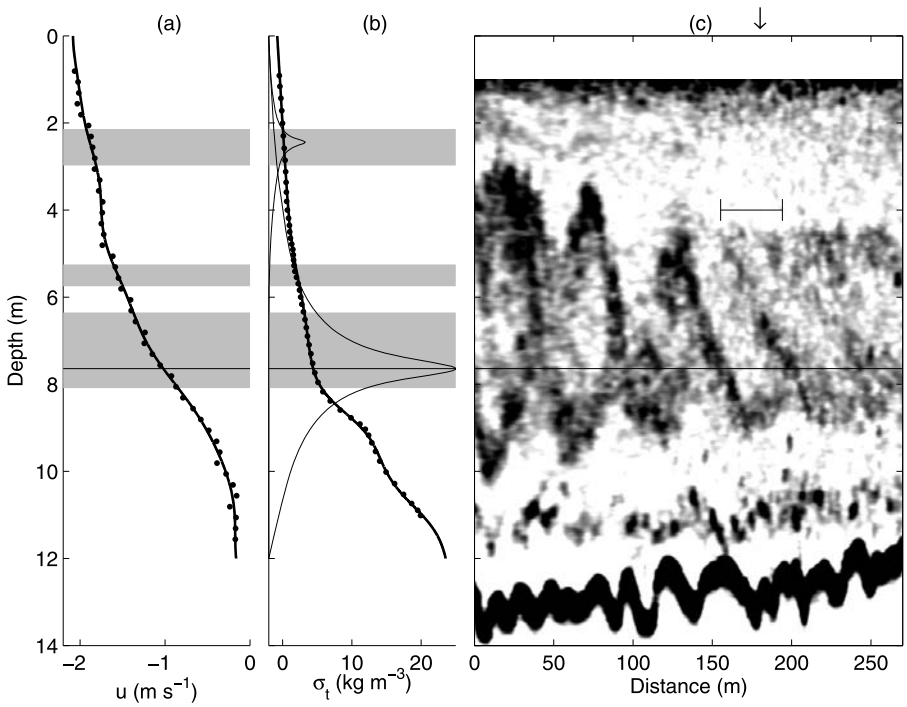

Figure 5. (a) Velocity and (b) density profiles observed during transect 1 (12 June 2006, 0805 LT, 8.9 km upstream of Sand Heads). The smooth profiles used in the stability analysis are shown as thick black lines, and the observed data are plotted as points. The gray shading indicates regions in which $Ri < 1/4$. The black horizontal line indicates the location of maximum displacement ($|\hat{\eta}|$) for the most unstable mode predicted with the TG equation. The thin lines in Figure 5b show the displacement functions for each of the unstable modes. The functions are scaled in proportion to the growth rate. (c) A close up of the echo sounding logged near the location of the profiles is shown and includes a scale indicating the apparent wavelength predicted by the TG equation. The arrow at the top of image indicates the approximate location of the density and velocity measurements. In this case, the velocity is averaged over a distance of approximately 130 m.

Here v_b is the velocity of the boat and c_r and λ are the phase speed and wavelength predicted with the TG equation. The predicted apparent wavelength, λ^*, is directly comparable to observations made from the moving boat. *Seim and Gregg* [1994] used a similar approach for estimating the wavelength of observed features.

[26] As well as giving a wavelength, phase speed, and growth rate for each unstable mode, the TG solutions also give an eigenfunction that describes the vertical structure of the growing mode. The vertical displacement eigenfunction $\hat{\eta}(z) = -\hat{\psi}/(U - c)$ is particularly useful. At the location in z where $|\hat{\eta}|$ is a maximum we expect to see evidence of instabilities in the echo soundings.

5. Results

[27] In this section we use J, $Ri(z)$ and solutions of the TG equation to assess the stability of six sets of velocity and density profiles (one from each of the six transects). Each set of profiles was chosen to coincide with evidence of instability in the echo soundings.

5.1. Ebb During High Discharge: Transect 1

[28] The selected velocity and density profiles from transect 1 are shown in Figure 5. The corresponding value of J for these profiles is 0.29 (see Table 1). The stability analysis yields two modes of instability. The fastest growing mode is unstable for wavelengths greater than 11 m and has a peak growth rate of 0.025 s^{-1} (doubling time of 28 s) occurring at a wavelength of 21 m. The phase speed of the instability at this wavelength is -1.02 m s^{-1}, where the negative indicates a seaward direction. Given this phase speed and the seaward drift of the boat (-2.2 m s^{-1}), an apparent wavelength of 39 m is calculated.

[29] Echo soundings collected at the same time, Figure 5c, show clear evidence of instabilities. The prediction is found to be similar to, although shorter than, the approximately 50 m wavelength of the observed instabilities. The maximum displacement of the predicted instabilities is located at a depth of 7.6 m (indicated by the horizontal line), closely matching the depth of the observed instabilities. Both the observed and predicted instability occur within the region of shear above the maximum gradient in ρ (at a depth of 9 m). As indicated by the gray shading, this region of high shear and low gradient in ρ corresponds to $Ri < 1/4$.

[30] For the set of profiles shown in Figure 5 the TG equation predicts a second, weaker, unstable mode located at a depth of 2.5 m. This mode is associated with the inflection point ($d^2 U/dz^2 = 0$) in the velocity profile at this depth. Because there is very little density stratification and

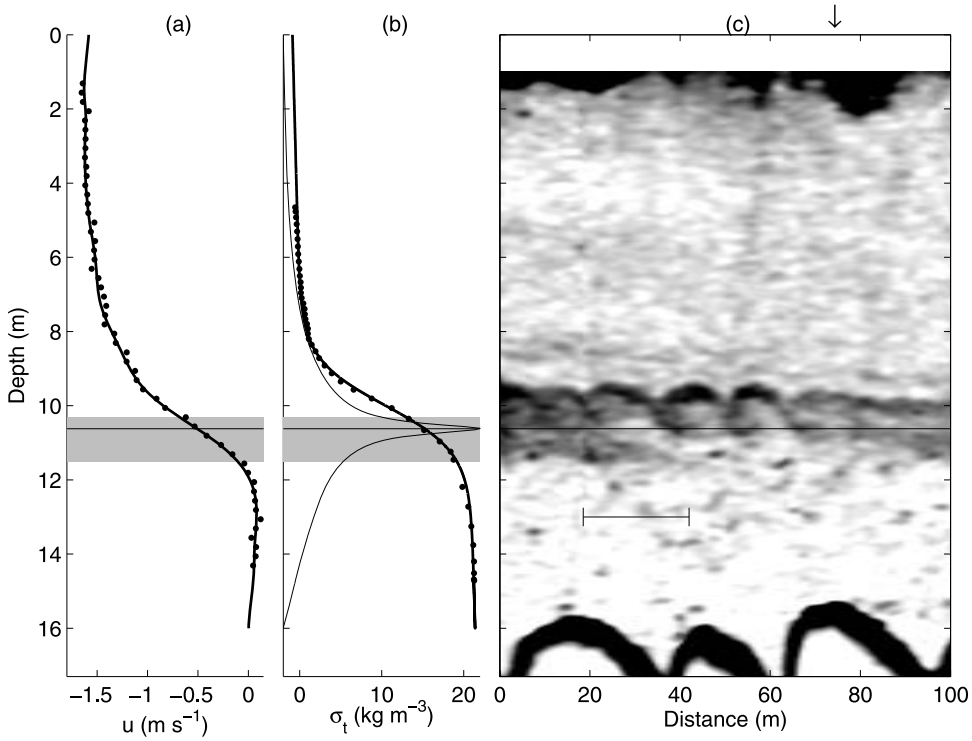

Figure 6. (a) Velocity and (b) density profiles observed during transect 2 (14 June 2006, 0821 LT, 11.1 km upstream of Sand Heads). See Figure 5 for details. In this case, the velocity is averaged over approximately 110 m.

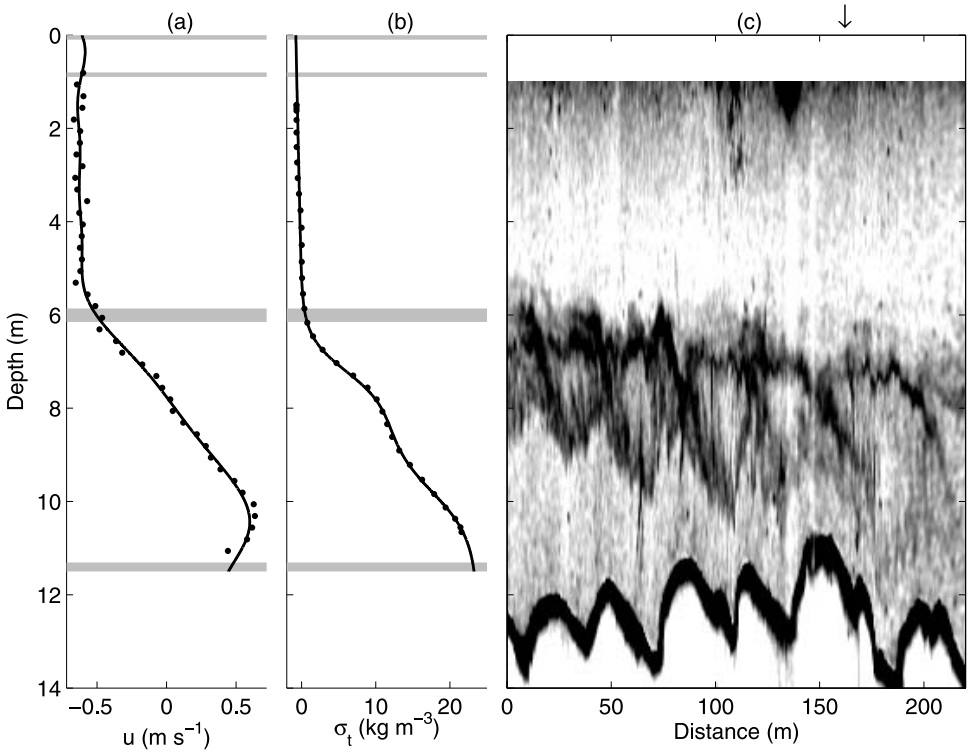

Figure 7. (a) Velocity and (b) density profiles observed during transect 3 (21 June 2006, 1238 LT, 2.66 km upstream of Sand Heads). See Figure 5 for details. In this case, the velocity is averaged over approximately 30 m.

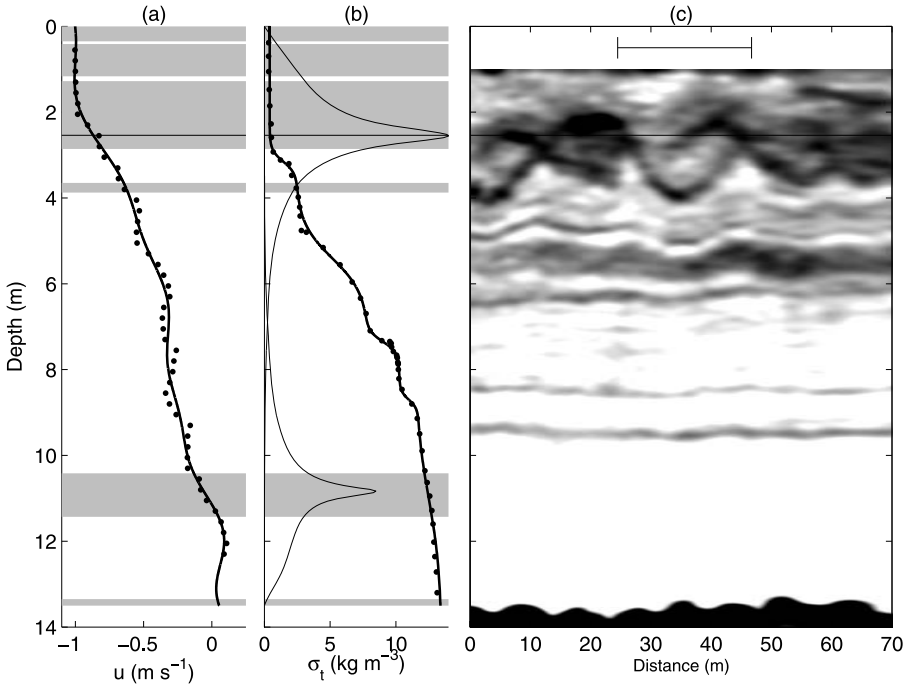

Figure 8. (a) Velocity and (b) density profiles observed during transect 4 (10 March 2008, 1120 LT, 22.4 km upstream of Sand Heads). See Figure 5 for details. In this case, the velocity is averaged over approximately 90 m.

hence weak echo intensity at this depth we are unable to confirm or deny the presence of this mode in the echo soundings.

5.2. Ebb During High Discharge: Transect 2

[31] In transect 2 a single hyperbolic tangent gives a good fit to the measured density profile (Figure 6b). Because of difficulties in profiling, the density profile at this location was missing data below 12 m. Data from the previous cast, taken 60 m upstream, were used below 12 m. This cast is expected to be sampling water of similar density below this depth.

[32] In this case the stability analysis of the profiles results in a single mode of instability. The mode is unstable for wavelengths from 10 m to 35 m with a peak growth rate of 0.02 s^{-1} (doubling time of 35 s) occurring at a wavelength of 17 m. The phase speed of the instability at this wavelength is -0.51 m s^{-1}. Given the drift velocity of -1.9 m s^{-1}, an apparent wavelength of 24 m is calculated. This prediction is found to be similar to, although longer than, the approximately 18 m wavelength of the small instabilities appearing in the echo sounding (Figure 6c). The maximum displacement of the predicted instabilities is located at a depth of 10.6 m, closely matching the depth of the observed instabilities.

5.3. Flood During High Discharge: Transect 3

[33] Despite the occurrence of $Ri < 1/4$ the stability analysis of the profiles in Figures 7a and 7b does not find any unstable modes. Echo soundings collected during the flood generally show features on the pycnocline that were well correlated with sand waves (Figure 7c). These correlated features are likely controlled by the hydraulics of the flow over the sand waves.

[34] There was very little evidence of instabilities independent of these sand waves. There appear to be some wave-like features on the pycnocline that are shorter ($\approx$10 m) than the sand waves, however, these are not well resolved by the echo sounder (e.g., depth of 9 m at x = 60 m). Properly assessing the flow over these sand waves would require at least two or three sets of density and velocity profiles per sand wave, more than we were able to obtain.

5.4. Low Freshwater Discharge

5.4.1. Early Ebb During Low Discharge: Transect 4

[35] At low discharge, during the ebb tide, shear and density stratification are spread over the entire depth (see Figure 4). The bulk shear layer thickness, h, is therefore greater than at high discharge, where shear and stratification were concentrated at a single, relatively thin interface. The increase in the vertical extent of the shear results in a greater bulk Richardson number despite a decrease in the overall strength of the density stratification, $\Delta\rho$ (see Table 1).

[36] The density and velocity profiles collected early in the ebb (transect 4, Figure 8) consist of a number of layers. The stability analysis yields two modes of instability. The most unstable mode has a peak growth rate of 0.023 s^{-1} occurring at a wavelength of 10.3 m with a phase speed of -0.86 m s^{-1}. Given this phase speed and the seaward drift of the boat (1.6 m s^{-1}), an apparent wavelength of 22 m is calculated. This is very similar to the wavelength of the largest instability in Figure 8c. This mode has a maximum displacement at a depth of 2.5 m, closely matching the location of the observed instabilities.

5.4.2. Mid Ebb During Low Discharge: Transect 5

[37] The instabilities in Figure 9c were observed 1 h later and approximately 3 km downstream from Transect 4. The ρ profile (Figure 9b) again displays a number of layers

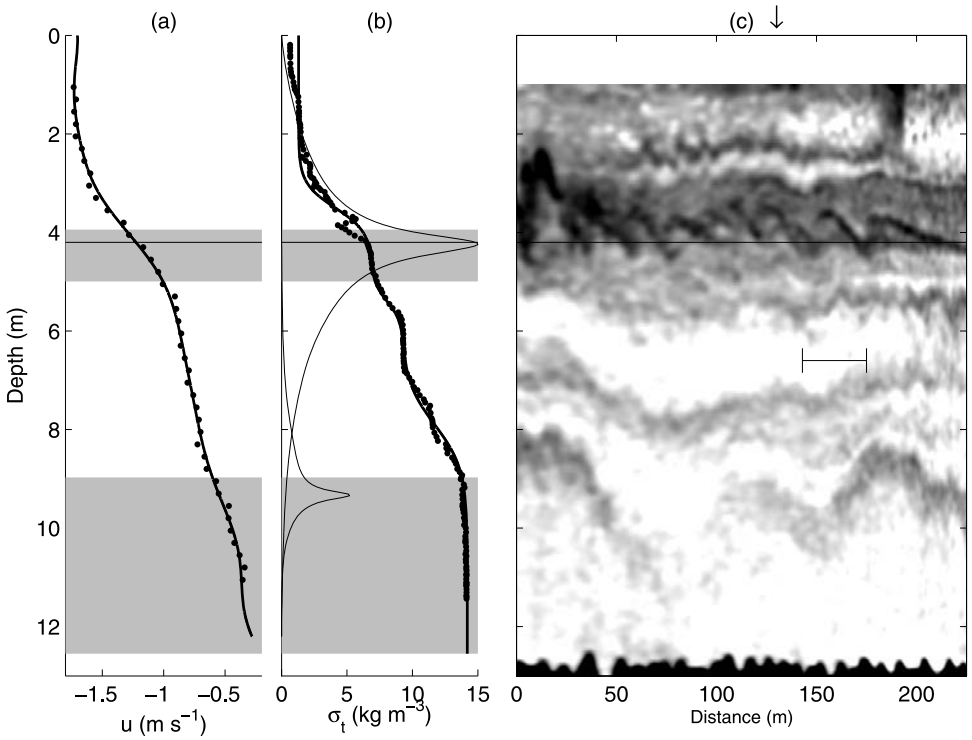

Figure 9. (a) Velocity and (b) density profiles observed during transect 5 (10 March 2008, 1221 LT, 19.6 km upstream of Sand Heads). See Figure 5 for details. In this case, the velocity is averaged over approximately 140 m.

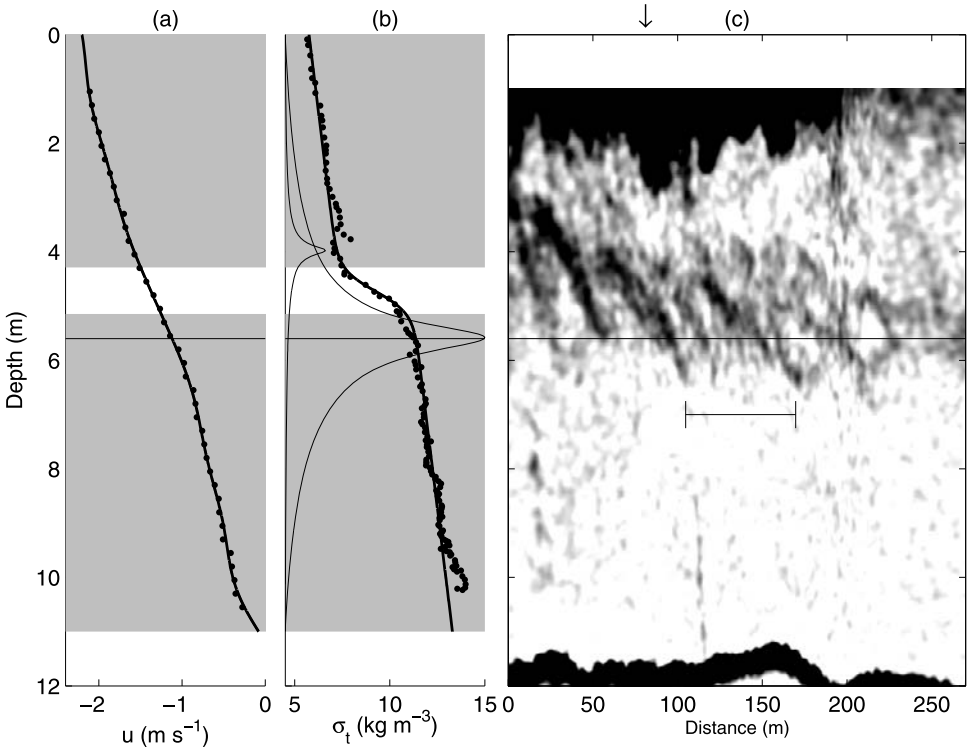

Figure 10. (a) Velocity and (b) density profiles observed during transect 6 (10 March 2008, 1434 LT, 7.6 km upstream of Sand Heads). See Figure 5 for details. In this case, the velocity is averaged over approximately 130 m.

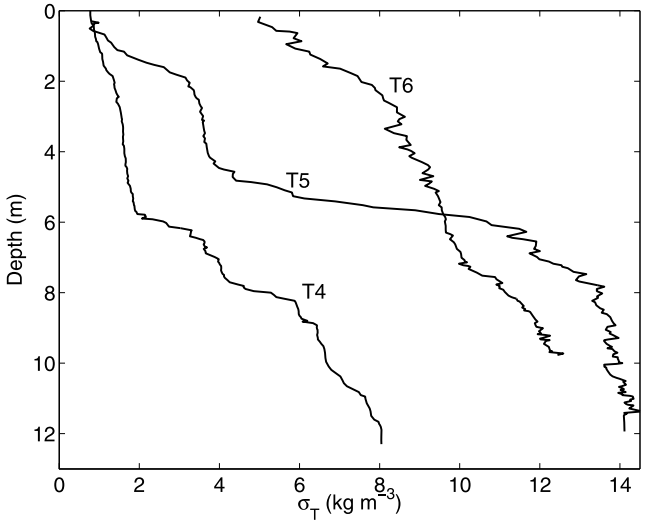

Figure 11. Selected density profiles from transects performed at low freshwater discharge. The profiles were collected at t = 10h53, 12h36, and 14h25 at x = 26.2, 17.9, and 8.8 km (transects 4, 5, and 6, respectively).

consisting of high-gradient steps. However, the layers are not evident in the measured velocity profile (Figure 9a), as was the case in Figure 8, and the overall shape of the velocity profile is more linear.

[38] The CTD cast is one of the few collected during the study where the instrument passed through an overturn in the pycnocline (depth of approximately 3.8 m). Consistent with the small amplitude of the instabilities in the echo sounder, the overturn in the density profile has only water of intermediate density; that is, no surface or bottom water is observed in the overturn.

[39] The TG equation predicts an unstable mode with a peak growth rate (0.03 s^{-1}) at a wavelength of 14 m with a phase speed of -1.2 m s^{-1}. The apparent wavelength is predicted to be 32 m, whereas the features in the echo sounder range in horizontal length from approximately 10 to 40 m, with the largest being near the TG prediction ($\approx$30 m). The predicted maximum in the displacement eigenfunction occurs at a depth of 4.2 m closely matching the depth of the instabilities.

5.4.3. Late Ebb During Low Discharge: Transect 6

[40] In the later stages of the ebb, during transect 6 (Figure 10), the shear has increased such that J is reduced to approximately 0.3. Unlike most of the other profiles collected during low or high discharge the density profile has no homogeneous layers, and shows small-scale (i.e., on the scale of the instrument resolution) overturning throughout the depth. In these profiles Ri is below critical throughout most of the depth aside from at the density interface.

[41] The most unstable mode predicted with the TG equation is located at a depth of 5.6 m and has a maximum growth rate of 0.019 s^{-1} at an apparent wavelength of 65m. This is close to, but longer than, the largest features in the echo sounder (approximately 50 m).

6. Small-Scale Overturns and Bottom Stress

[42] In Figure 10 there are no features in the echo soundings that are associated with the small-scale overturns in ρ below a depth of 7 m, and although our solutions to the TG equation suggest unstable modes, these are both located well above a depth of 7 m. To further examine the source of these overturns we compare selected density profiles from each of the low discharge transects (Figure 11). In the density profile from transect 4, small-scale overturns are rare or completely absent (Figure 11, T4). Approximately 2 h later, during transect 5, just one profile exhibits these small-scale overturns (Figure 11, T5). This cast was performed at the shallow constriction in the river associated with the Massey Tunnel (Figure 4b, 18 km). In this case the small-scale overturns in the profile occur only below the pycnocline suggesting that the stratification within the pycnocline is confining the overturns to the lower layer. By maximum ebb, small-scale overturns occur throughout the depth (Figure 11, T6).

[43] The presence of these small-scale overturns is apparent, although not immediately obvious, in the echo soundings in Figure 4. Note that the scale of the shading is the same in Figures 4a–4c and that there is a gradual increase (darkening) in background echo intensity from early to late ebb (transects 4 to 6). This increase in echo intensity is attributed to the small-scale overturning observed in the density profiles. Early in the ebb the dark shading associated with high echo intensity is concentrated at the density interfaces (transect 4). Otherwise, at this time, echo intensity is low (light shading) corresponding to an absence of small-scale overturns in the density profiles (e.g., Figure 11, T4). At this stage of the ebb, near-bottom velocities are close to zero and bottom stress is expected to be negligible. In transect 5 (Figure 4b) there is an increase in echo intensity as the flow passes over the Massey Tunnel (18 km). At this location and during this stage of the ebb, near bottom velocity increases to approximately 0.2 m s^{-1} at 1 m above the bed. In this case the small-scale overturns in the profile occur only below the pycnocline (Figure 11, T5) suggesting that the stratification within the pycnocline is confining bottom generated turbulence to the lower layer. Near maximum ebb, during transect 6, near bottom velocities reach 0.5 m s^{-1} at 1 m above the bed. By this stage, high echo intensity and small-scale overturns occur throughout the depth (Figure 11, T6) suggesting that bottom generated turbulence has reached the surface despite the presence of stratification.

7. Discussion

[44] Although combining echo soundings, velocity, and density measurements to study shear flows is not in itself novel, even for studies in the Fraser estuary [e.g., *Geyer and Smith*, 1987], efforts in the present study were focussed on simultaneously measuring the details of the flow and the shear instabilities. Our strategy of drifting slowly with the upper level flow allowed acoustic imaging to capture shear instabilities similar to those observed in laboratory and numerical simulations [e.g., *Tedford et al.*, 2009]. Density and velocity measurements also allowed us to analyze these features using a method more typically applied to laboratory experiments, namely direct application of the TG equation. This analysis has refined our understanding of instability and mixing in the Fraser River estuary.

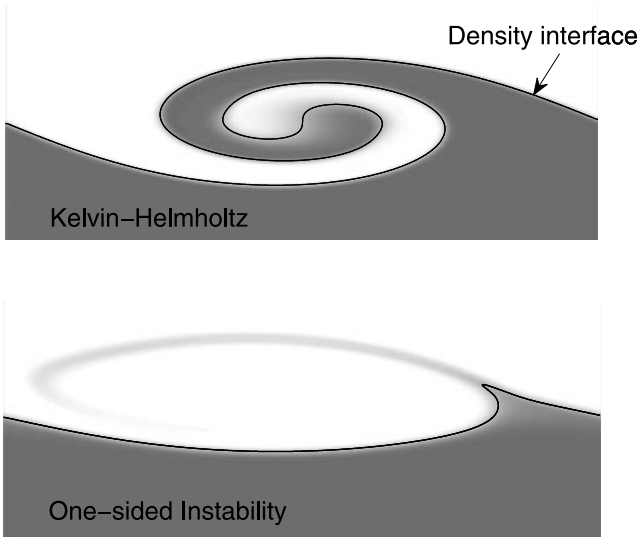

Figure 12. Schematic of a Kelvin-Helmholtz and a one-sided instability. The gray shading indicates mixed fluid, and the solid black line indicates the position of the central isopycnal (i.e., density interface).

7.1. One-Sided Instability

[45] In all five of the cases that the TG equation predicted the occurrence of unstable modes, the bulk Richardson number, J, was greater than 1/4. This result suggests the mixing layer model and associated J (see section 4.3) are not adequate for describing the stability of the measured profiles. In all of these unstable cases, both the region of $Ri(z) < 1/4$ and the depth of the maximum in the displacement eigenfunction ($|\hat{\eta}(z)|$) were vertically offset from the maximum gradient in density ($d\rho/dz$). This offset between the depth of the predicted region of instability and the density interface is due to asymmetry between the density and velocity profiles. This suggests that a minimum of three bulk parameters (J, R, a) are required if the stability is to be represented by the simplified profiles of equation (2).

[46] Laboratory models and direct numerical simulations (DNS) of asymmetry result in one-sided instabilities that resemble the features in the echo soundings in Figures 5c, 6c, and 8c [e.g., *Lawrence et al.*, 1991; *Yonemitsu*, 1991; *Carpenter et al.*, 2007]. Similar observations were made in the Strait of Gibraltar by *Farmer and Armi* [1998] and in a strongly stratified estuary by *Yoshida et al.* [1998]. In these cases the instabilities were attributed to one-sided modes. One-sided modes are part of a general class of instability that includes the Holmboe mode. In contrast to the classic KH mode, the Holmboe mode is a result of the unstable interaction of gradients in density and gradients in shear (N^2 and $d^2\ U/dz^2$ in equation (1)) and can occur at relatively high values of J [*Holmboe*, 1962].

[47] There are a number of potential sources of asymmetry in the Fraser estuary. The most obvious is the difference in the bottom and surface boundary condition. If the stress acting on these boundaries is not equal and opposite, i.e., if it is unbalanced, then there is the potential for asymmetry. During low freshwater discharge the presence of multiple layers of varying thickness adds further irregularity and potential asymmetry to the profiles. Although some laboratory models of stratified flows successfully generate symmetric conditions [e.g., *Thorpe*, 1973; *Tedford et al.*, 2009], many others result in asymmetry [e.g., *Lawrence et al.*, 1991; *Yonemitsu et al.*, 1996; *Pawlak and Armi*, 1998; *Zhu and Lawrence*, 2001]. In most of these cases asymmetry in the flow results from the geometry of the channel, such as a sill causing localized acceleration of the lower layer. In the arrested salt wedge experiments of *Yonemitsu et al.* [1996], asymmetry was associated with secondary circulation. Given the common occurrence of asymmetry in the laboratory it is not surprising to find asymmetry in nature.

7.2. Mixing

[48] Linear stability analysis does not provide quantitative predictions of mixing. When one-sided instabilities are modeled using DNS at the values of J observed here the complete overturning of the density interface normally associated with KH billows does not occur. Figure 12 shows a schematic of a one-sided instability and a Kelvin-Helholtz instability. Although one-sided instabilities are offset from the region of maximum density gradient they have been found to be responsible for considerable mixing [*Smyth and Winters*, 2003; *Carpenter et al.*, 2007]. Unlike the mixed fluid that results from the KH instability, the mixed fluid that results from one-sided instabilities is not concentrated at the density interface, but, is instead drawn away from the density interface [*Carpenter et al.*, 2007].

[49] *MacDonald and Horner-Devine* [2008] quantified mixing in the Fraser estuary at high freshwater discharge over approximately two tidal cycles. Using a control volume approach and overturning analysis they estimated mean buoyancy flux, B, during the ebb to be 2.2×10^{-5} m^{2}s^{-3}. The associated mean turbulent eddy diffusivity, $K = B/N^2$, was estimated to be 9×10^{-4} m^2 s^{-1} [*MacDonald*, 2003]. *Smyth et al.* [2007] proposed parameterizing the mixing caused by Holmboe instabilities as $K = 0.8 \times 10^{-4}\ h\Delta U$. For transect 1 of the present study, which most closely matches the conditions of *MacDonald and Horner-Devine* [2008] (see Table 1), this results in $K = 6.7 \times 10^{-4}$ m^2 s^{-1} ($0.8 \times 10^{-4} \times 5.2$ m $\times$ 1.6 m s^{-1}). The parametrization of *Smyth et al.* [2007] represents the effect of a uniform distribution of instabilities and has not been validated at high Reynolds number. Mindful of these inherent limitations of DNS and the complexity of the field conditions, the similarity between the observed ($K = 9 \times 10^{-4}$ m^2 s^{-1}) and predicted mixing ($K = 6.7 \times 10^{-4}$ m^2 s^{-1}) is promising. A more rigorous analysis would include a description of the spatial and temporal distribution of instabilities. Unfortunately, our sampling was inadequate to comprehensively describe this distribution particularly at high freshwater discharge.

[50] During our survey of the estuary the mixing was apparently caused by shear instabilities acting within the interior of the flow and, to a lesser extent, by turbulence associated with the bottom boundary. Although we have addressed these two types of mixing separately they both originate as a shear instability. Unlike instability predicted with the TG equation the instability associated with the bottom boundary layer relies on viscous effects and the presence of the solid boundary. In some cases, for example during late ebb at low freshwater discharge (transect 6, Figure 10), the two mechanisms (TG-type instabilities and

viscous shear instabilities) are acting together to generate mixing.

[51] At high freshwater discharge, during the ebb, *MacDonald and Horner-Devine* [2008] found that mixing at the pycnocline causes a collapse of the salt wedge which leads to complete flushing of seawater from the estuary. The well defined salt wedge is then regenerated during the subsequent flood. Although we also see a well defined salt wedge at high discharge our observations at low freshwater discharge suggest that during the ebb mixing caused by both shear instabilities at the pycnocline and bottom generated turbulence is not able to homogenize the water column. We therefore expect the presence of mixed water in the estuary at the beginning of the subsequent flood. The presence of this mixed water will prevent the formation of a well defined salt wedge and the estuary will remain in a partially mixed state.

7.3. Wave Height

[52] Unlike KH instabilities, the deflection of the density interface (wave amplitude) caused by one-sided instabilities is usually smaller than the amplitude of the billows (see Figure 12). It is therefore difficult to assess the amplitude of the instabilities using echo soundings (e.g., Figure 5). Nevertheless, taking the vertical distance between the trough and the cusp, the observed instabilities vary in height from approximately 0.5 m to 2 m. The maximum height to wavelength aspect ratio of the observed instabilities varies between approximately 0.025 (0.5/20, Figure 6c) and 0.1 (2/20, Figure 5c). In the tilting tube experiments of *Thorpe* [1973] the maximum aspect ratio of KH instabilities varied between 0.05 and 0.6. Given the low values of J (<1/4) in Thorpe's experiments this difference in aspect ratio is not surprising. Unfortunately, other than the case of the KH instability (symmetric density and velocity profiles and $J <$ 1/4) the height of shear instabilities in stratified flows is not well documented.

7.4. Use of Echo Soundings to Identify Instability

[53] Our analysis focused on periods when instabilities were evident in the echo soundings. There were instances where predictions from the TG equation suggested instabilities would occur, but none were visible in the echo sounder. In some cases (e.g., the secondary mode in Figure 5), the lack of apparent instabilities in the echo soundings can be explained by the absence of the strong variations in salinity and temperature (i.e., density stratification) that are responsible for most of the back scatter of sound to the instrument (for a thorough description of acoustic scattering in similar environments, see *Seim* [1999] and *Lavery et al.* [2003]).

[54] The quality of the visualization of the instabilities also depends on the speed of the boat relative to the speed of the instabilities. For profiles collected at 2.2 km, during transect 3 (Figure 3c), the TG equation predicted instability close to the depth of the pycnocline (results not shown). In this region the boat speed and predicted instability speed were almost the same (-0.28 m s^{-1} versus -0.24 m s^{-1}). Considering equation (3), the resulting apparent wavelength would be 250 m. The corresponding apparent period of approximately 15 min (250 m/-0.28 m s^{-1}) would likely distort the appearance of an instability beyond recognition. This highlights an important challenge in identifying instabilities in echo soundings: if the point of observation is moving at a speed similar to the instabilities, the appearance of the instabilities becomes greatly distorted. On the other hand, if the observer is moving at a much different velocity than the instabilities; that is, the apparent wavelength and period are relatively short, the sampling rate of the echo sounder may not be sufficient to resolve the instabilities.

[55] In addition, our ability to detect shear instabilities depends on the timing of the echo sounding relative to the stage of development of the instability. In DNS of symmetric and asymmetric instabilities, there are several stages of development beginning with rapid growth and finishing with a breakdown into three-dimensional turbulence. Only during the stage where the instabilities have large two-dimensional structures, for example, billows, will they be easily recognizable with the echo sounder. For example, during transect 2 (Figure 3b) instabilities were only recognizable over a distance of approximately 100 m (11 to 11.1 km). However it is possible that instabilities are at a less recognizable stage of development throughout most of this transect.

[56] Because of these challenges, the echo sounder is able to confirm only the presence and not the absence of shear instability. We therefore limited our application of the TG equation to cases where instabilities were apparent.

8. Conclusions

[57] After performing a detailed stability analysis on six sets of velocity and density profiles using the Taylor-Goldstein equation and comparing with the echo soundings we conclude the following.

[58] 1. All of the instabilities observed in the echo soundings coincided with the most unstable mode in the TG analysis. This confirms the applicability of the TG equation in predicting instability, even in cases as complex as the Fraser River estuary.

[59] 2. The location of each of the observed instabilities occurs in a region of depth where $Ri < 1/4$. However, there are also cases that have $Ri < 1/4$ in which no unstable modes were observed. This result is in full agreement with the Miles-Howard criterion, but also highlights the inconclusive nature of this criterion.

[60] 3. Although the observed instabilities all act on a well defined density interface, they appear to be concentrated on only one side of the interface. The maximum vertical displacement occurs either above or below the density interface in a region of z where $Ri < 1/4$. None of the observations show $Ri < 1/4$ across the thickness of a density interface. This is in contrast to the archetypal KH instability described by the simple mixing layer model, in which $Ri < 1/4$ where $d\rho/dz$ (N^2) is greatest. The observed instabilities might therefore be better described by the so-called "one-sided" modes of *Lawrence et al.* [1991] and *Carpenter et al.* [2007].

[61] 4. During the majority of the survey the observed mixing was due to shear instabilities at the pycnocline. In other stratified estuaries with moderate to strong tidal forcing, such as the Columbia and Hudson rivers, turbulence generated at the bottom is considered the dominant source of mixing [*Peters and Bokhorst*, 2000; *Nash et al.*,

2009]. In the present study we only observe mixing due to bottom generated turbulence during late ebb at low freshwater discharge.

[62] **Acknowledgments.** The authors thank NSERC for grants 36366-06 and 194270-06. Gregory Lawrence is also grateful for the support of a Canada Research Chair. We would also like to thank Bill Smyth for providing us with the TG code and for helpful discussions and Melissa Rohde for assistance with the field program.

References

Alexakis, A. (2005), On Holmboe's instability for smooth shear and density profiles, *Phys. Fluids*, *17*, 084103, doi:10.1063/1.2001567.

Carpenter, J., G. Lawrence, and W. Smyth (2007), Evolution and mixing of asymmetric Holmboe instabilities, *J. Fluid Mech.*, *582*, 103–132.

Farmer, D., and L. Armi (1998), The flow of Atlantic water through the Strait of Gibraltar, *Prog. Oceanogr.*, *21*, 1–98.

Geyer, W., and D. Farmer (1989), Tide-induced variation of the dynamics of a salt wedge estuary, *J. Phys. Oceanogr.*, *19*, 1060–1672.

Geyer, W., and J. Smith (1987), Shear instability in a highly stratified estuary, *J. Phys. Oceanogr.*, *17*, 1668–1679.

Goldstein, S. (1931), On the stability of superposed streams of fluids of different densities, *Proc. R. Soc. London A*, *132*, 524–548.

Hazel, P. (1972), Numerical studies of the stability of inviscid stratified shear flows, *J. Fluid Mech.*, *51*, 39–61.

Holmboe, J. (1962), On the behavior of symmetric waves in stratified shear layers, *Geofys. Publ.*, *24*, 67–112.

Howard, L. (1961), Note on a paper of John W. Miles, *J. Fluid Mech.*, *10*, 509–512.

Kostachuk, R., and L. Atwood (1990), River discharge and tidal controls on salt-wedge position and implications for channel shoaling: Fraser River, British Columbia, *Can. J. Civ. Eng.*, *17*, 452–459.

Lavery, A., R. Schmitt, and T. Stanton (2003), High-frequency acoustic scattering from turbulent oceanic microstructure: The importance of density fluctuations, *J. Acoust. Soc. Am.*, *114*, 2685–2697.

Lawrence, G., F. Browand, and L. Redekopp (1991), The stability of a sheared density interface, *Phys. Fluids*, *3*, 2360–2370.

MacDonald, D. (2003), Mixing processes and hydraulic control in a highly stratified estuary, Ph.D. thesis, Mass. Inst. of Technol., Cambridge.

MacDonald, D., and A. Horner-Devine (2008), Temporal and spatial variability of vertical salt flux in a highly stratified estuary, *J. Geophys. Res.*, *113*, C09022, doi:10.1029/2007JC004620.

Miles, J. (1961), On the stability of heterogeneous shear flows, *J. Fluid Mech.*, *10*, 496–508.

Miles, J. (1963), On the stability of heterogeneous shear flows. Part 2, *J. Fluid Mech.*, *16*, 209–227.

Moum, J., D. Farmer, W. Smyth, L. Armi, and S. Vagle (2003), Structure and generation of turbulence at interfaces strained by internal solitary waves propagating shoreward over the continental shelf, *J. Phys. Oceanogr.*, *33*, 2093–2112.

Nash, J. D., L. F. Kilcher, and J. N. Moum (2009), Structure and composition of a strongly stratified, tidally pulsed river plume, *J. Geophys. Res.*, *114*, C00B12, doi:10.1029/2008JC005036.

Pawlak, G., and L. Armi (1998), Vortex dynamics in a spatially accelerating shear layer, *J. Fluid Mech.*, *376*, 1–35.

Peters, H., and R. Bokhorst (2000), Microstructure observations of turbulent mixing in a partially mixed estuary. Part 1: Dissipation, *J. Phys. Oceanogr.*, *30*, 1232–1244.

Seim, H. (1999), Acoustic backscatter from salinity microstructure, *J. Atmos. Oceanic Technol.*, *16*, 1491–1498.

Seim, H., and M. Gregg (1994), Detailed observations of naturally occurring shear instability, *J. Geophys. Res.*, *99*, 10,049–10,073.

Smyth, W. D., and K. B. Winters (2003), Turbulence and mixing in Holmboe waves, *J. Phys. Oceanogr.*, *33*, 694–711.

Smyth, W., J. Carpenter, and G. Lawrence (2007), Mixing in symmetric Holmboe waves, *J. Phys. Oceanogr.*, *37*, 1566–1583.

Taylor, G. (1931), Effect of variation in density on the stability of superposed streams of fluid, *Proc. R. Soc. London A*, *132*, 499–523.

Tedford, E., R. Pieters, and G. Lawrence (2009), Symmetric Holmboe instabilities in a laboratory exchange flow, *J. Fluid Mech.*, *636*, 137–153.

Thorpe, S. (1973), Experiments on instability and turbulence in a stratified shear flow, *J. Fluid Mech.*, *61*, 731–751.

Thorpe, S. (2005), *The Turbulent Ocean*, 1st ed., Cambridge Univ. Press, Cambridge, U. K.

Ward, P. (1976), Seasonal salinity changes in the Fraser River Estuary, *Can. J. Civ. Eng.*, *3*, 342–348.

Yonemitsu, N. (1991), Stability and waves of a salt-wedge flow, Ph.D. thesis, Univ. of Alberta, Edmonton, Alberta, Canada.

Yonemitsu, N., G. Swaters, N. Rajaratnam, and G. Lawrence (1996), Shear instabilities in arrested salt-wedge flows, *Dyn. Atmos. Oceans*, *24*, 173–182.

Yoshida, S., M. Ohtani, S. Nishida, and P. Linden (1998), Mixing processes in a highly stratified river, in *Physical Processes in Lakes and Oceans*, *Coastal Estuarine Stud.*, vol. 54, edited by J. Imberger, pp. 389–400, AGU, Washington, D. C.

Zhu, D., and G. Lawrence (2001), Holmboe's instability in exchange flows, *J. Fluid Mech.*, *429*, 391–409.

J. R. Carpenter, G. A. Lawrence, and E. W. Tedford, Department of Civil Engineering, University of British Columbia, Vancouver, BC V6T 1Z4, Canada. (ttedford@eos.ubc.ca)

R. Pawlowicz and R. Pieters, Department of Earth and Ocean Sciences, University of British Columbia, Vancouver, BC V6T 1Z4, Canada.